Climatology of High-frequency Gravity Waves Observed by an Airglow Imager at Andes Lidar Observatory

Bing Cao[1], Alan Z. Liu[2]

[1]Institute of Geophysics and Planetary Physics, Scripps Institution of Oceanography, University of California San Diego, La Jolla, CA, USA

[2]Center for Space and Atmospheric Research and Department of Physical Sciences, Embry-Riddle Aeronautical University, Daytona Beach, FL, USA

Key Points:

- A large number of high-frequency gravity waves were observed near mesopause region over the Andes by an airglow imager.
- Preferential propagation direction of the waves shows seasonal dependence, poleward in austral summer and equator-ward in austral winter.
- Convective activities are a likely wave source, playing an important role in shaping the observed wave directionality.

Corresponding author: Bing Cao, bic020@ucsd.edu

Abstract

The long-term climatology of high-frequency quasi-monochromatic gravity waves is presented using multi-year airglow images observed at Andes Lidar Observatory (ALO, 30.3°S, 70.7°W) in northern Chile. A large number of high-frequency gravity waves were retrieved from OH airglow images. The distribution of primary wave parameters including horizontal wavelength, vertical wavelength, intrinsic wave speed, and intrinsic wave period are obtained and are in the ranges of 20–30 km, 15–25 km, 50–100 ms^{-1}, and 5–10 min, respectively. The waves tend to propagate against the local background winds and show clear seasonal variations. In austral winter (May–Aug), the observed wave occurrence frequency is higher and preferential wave propagation is equator-ward. In austral summer (Nov–Feb), the wave occurrence frequency is lower and the waves mostly propagate pole-ward. Critical-layer filtering plays an important role in determining the preferential propagation direction in certain months, especially for waves with a small observed phase speed (less than typical background winds). The wave occurrence and preferential propagation direction are shown to be related to the locations of convection activities nearby and their relative distance to ALO. However, other possible wave sources such as secondary wave generation and possible ducted propagation cannot be ruled out. The estimated momentum fluxes have typical values of a few to 10 m^2s^{-2} and show seasonal variations with a clear anti-correlation with local background wind directions.

1 Introduction

Airglow refers to the emissions of photons in the Earth atmosphere via chemiluminescence processes, that mainly result from the reactions among species such as atomic oxygen, atomic nitrogen, and hydroxyl radicals (Khomich et al., 2008). Several of these emissions originate within the Mesosphere and Lower Thermosphere (MLT) region (altitude range around 80–100 km) as thin luminous layers with typical thickness of 6–10 km (Full Width at Half Maximum, or FWHM). Historically, the first airglow emissions to be investigated were the green ionized oxygen (OI) line (557.7 nm) with peak altitude at ∼96 km and the yellow Na line (589.2 nm) with peak altitude at ∼90 km. But the brightest source of airglow is the hydroxyl (OH) Meinel bands emission (peak altitude at ∼87 km) which radiates over a broad spectral range (0.7–4.0 µm) primarily in the near-infrared band. Many studies have revealed that these airglow emissions are very useful tracers to retrieve the atmospheric properties and study the dynamical processes such

as instabilities, ripples, small scale gravity waves, as well as larger scale atmospheric waves such as tides and planetary waves (e.g., Medeiros et al., 2007; T. Li et al., 2009; Cao et al., 2016; J. Li et al., 2017).

The atmospheric flow in the MLT region is dominated by abundant atmospheric waves, of which gravity waves are an important type with large varieties in wave characteristics and potential sources. High-frequency atmospheric gravity waves carry significant amount of momentum from lower atmosphere. The dissipation and breaking of these waves have large impacts to the circulation through momentum deposition to the background flow. Airglow imaging systems are most sensitive to this part of gravity waves spectrum because of the high horizontal and temporal resolution (J. Hecht et al., 2001; Ejiri et al., 2003; J. H. Hecht et al., 2004). Gravity wave information can be inferred from the wave induced emission intensity fluctuations detected by such imaging systems. These gravity waves are revealed with typical horizontal wavelengths of 20 to 100 km, intrinsic wave periods of 5 to 10 min, and horizontal phase speeds between 30 to 100 ms^{-1} (Taylor, 1997; Ejiri et al., 2003; Z. Li et al., 2011). The momentum flux estimated from airglow emission perturbation has an average magnitude of 5–10 m^2s^{-2} (J. Tang, Kamalabadi, et al., 2005; Y. Tang et al., 2014). Studies based on airglow observations suggest that the wave propagation in the mid-latitudes often shows an annual variation: pole-ward in summer and equator-ward in winter. Several mechanisms such as critical layer filtering (Taylor et al., 1993), ducted wave propagation (Walterscheid et al., 1999), variations of the location of wave sources (Nakamura et al., 2003) and Doppler-shift by the background winds (Z. Li et al., 2011) were proposed to explain the directionality of wave propagation. In general, these mechanisms all play some roles in affecting the wave propagation directions but their relative importance varies with seasons and geographic locations.

Andes Lidar Observatory (ALO) is located at Cerro Pachón (30.3°S, 70.7°W) on the west side of Andes ridge, which is generally aligned in the north-south direction and extends several thousands kilometers in South America. The elevation of ALO is 2530 m compared to the ridge peak altitude of 4500–5000 m. Many satellite observations have revealed the existence of gravity wave hot spots in the stratosphere over southern Andes (Hoffmann et al., 2013; Hindley et al., 2015). It is believed that the major wave sources are subtropical deep convection in low and mid-latitude, and orographic sources at latitudes of 40°S to 70°S during austral winter time (Jiang et al., 2004). Whether these ac-

tive gravity waves in stratosphere reach higher MLT region before they break remains an unanswered question. Airglow imaging systems, together with other observation instruments, have been utilized to depict a complete picture of gravity wave propagation from stratosphere to mesosphere (Bossert et al., 2014; Fritts et al., 2019; Taylor et al., 2019). By comparing the results with previous deployment of airglow imager at other locations, the similarities as well as differences of wave characteristics, preferential propagation directions, and momentum flux may reflect the generality and specialty of wave sources and background winds at different locations.

In this study, we present an application of the long-term dataset of mesospheric airglow and wind observations that were acquired in the Andes. The dataset is used to study the distribution of the intrinsic gravity wave parameters, their dominant propagation directions and possible controlling mechanisms, as well as variation of momentum flux and its relationship with background wind. The study is organized as following: section 2 briefly describes the instrumentation from which the data were retrieved and section 3 describes the dataset and methodology. Sections 4 and 5 present the main results and discussion. The summary and conclusions are presented in section 6.

2 Instrumentation

2.1 Airglow Imager

An all-sky airglow imager is equipped with a cooled charge-coupled device (CCD) and a fish-eye lens to collect the airglow emissions from all the sky. One or several narrow width bandpass filters are used to distinguish the emissions of different spectrum range from different altitude ranges (Taylor et al., 1995). The airglow imager operated at ALO was equipped with two filters to capture OH and OI emissions alternately at night during the low moon period throughout the year. The integration times for the OH and OI images are 1 min and 1.5 min, respectively. For OH Meinel band emission, the bandwidth of the filter is 750–930 nm with a notch at 865 nm to exclude the molecular oxygen emission. The airglow emissions were collected by a 1024 $\times$ 1024 CCD array and then binned to a 512 $\times$ 512 array to increase signal-to-noise ratio. When the field-of-view is limited within $\pm 45^{\circ}$ zenith angle, the airglow images cover an area of about 200$\times$200 km^2 with a resolution better than 1 km/pixel if projected to OH airglow altitude at $\sim$87 km.

2.2 Meteor Radar

The ALO meteor radar uses a SKiYMET radar system (Franke et al., 2005) operating at 40.92 MHz. There are two major components of the radar. The transmitter is a three-element Yagi antenna directed toward the zenith with a transmitted power of approximately 170 W from a 13.3 µm pulse length, 6 kW peak envelop power and 466 µm inter-pulse period. The meteor trails were illuminated by the radiated energy. The receiver is comprised of five three-element Yagi antenna oriented along two orthogonal baselines and they sampled every 13.3 µm, resulting in 2 km range resolution. The backscattered signals from meteor trail are received by different antennas at different arrival angle and timing. Then, the interferometry method was performed to determine the position of meteor trail in the sky. Wind velocities were retrieved from the continuous tracking of trail positions and Doppler shifts (Hocking et al., 2001) with the assumption that the horizontal wind field is almost uniform and stationary within the spatio-temporal window and the vertical wind is negligible. The meteor radar provides continuous hourly-averaged horizontal winds between 80 and 100 km (Franke et al., 2005). The winds around the OH airglow layer were calculated through Gaussian-weighted averaging centered at 87 km with a window of 5 km.

3 Data and Methodology

A narrow-band sodium wind/temperature lidar, an all-sky airglow imager, a photometer, and a meteor radar have been deployed to ALO since September 19, 2009. The airglow imager captured only OH images before Aug 2011, OH and OI images alternately after that. The possible influence of the different image timing on wave extraction is discussed in details in Supporting Information. The meteor radar had some technical issues in mid 2014, thus no more wind data were observed afterwards. Therefore, we only processed the airglow data when the meteor radar wind data were available (2009 to 2014). The number of hours when OH airglow images were obtained are summarized in Table 1. There are about 300–600 hours of data in each calendar month accumulated in 6 years. The amount of data enables a robust analysis of seasonal variations of gravity waves.

Before airglow images can be used for wave extraction, there are several pre-processing procedures that need to be implemented. Firstly, all the stars present on the images need be removed. Secondly, images need to be unwrapped to correct the spatial distortions due to fish-eye lens and emission intensity variation due to van Rhijn effect. Thirdly, the Milky Way over ALO in southern hemisphere is present and close to zenith most of the time and is much brighter than the airglow emission within the imager observational bandwidth. Therefore, an additional procedure of removing the Milky Way (Z. Li et al., 2014) is necessary and applied before gravity waves can be identified.

High frequency, quasi-monochromatic gravity waves are identified from the images using a series of procedures described in detail in J. Tang, Franke, et al. (2005) and J. Tang, Kamalabadi, et al. (2005) and briefed here. Three consecutive images (I_1, I_2, I_3) were used to form two consecutive time-differenced (TD) images ($TD_1 = I_2 - I_1$, $TD_2 = I_3 - I_2$) for spectral analysis. Horizontal wave parameters including wavelength, observed phase speed, propagation direction and relative airglow perturbation amplitude ($I'_{OH}/\overline{I}_{OH}$) were derived from each set of two TD images. Intrinsic phase speed and intrinsic frequency are derived with background winds provided by meteor radar. Vertical wavelength is calculated using a simplified dispersion relationship (equation 24 of Fritts and Alexander (2003)) with buoyancy frequency near the OH airglow layer derived using temperature from NRLMSISE-00 empirical model (Picone et al., 2002). The relative airglow intensity amplitude is calculated by dividing the perturbation intensity I'_{OH} by the average intensity $\overline{I}_{OH}$ of the star-free and de-trended images after excluding the dark current and background emission, which is assumed to be 30% of total emission intensity (Swenson & Mende, 1994). The gravity wave momentum flux was derived based on the intrinsic wave parameters and relative temperature amplitude, converted from $I'_{OH}/\overline{I}_{OH}$ using the airglow model described in Liu and Swenson (2003). The total gravity wave momentum flux is calculated using the following equation:

$$F_m = \frac{k}{m}\frac{g^2}{N^2}\left\langle\left(\frac{T'}{\overline{T}}\right)^2\right\rangle = \frac{k}{m}\frac{g^2}{N^2C^2}\left\langle\left(\frac{I'_{OH}}{\overline{I}_{OH}}\right)^2\right\rangle \left(\mathrm{m^2 s^{-2}}\right), \tag{1}$$

of which k, m are the horizontal and vertical wavenumber, N^2 is the squared buoyancy frequency and C is the cancellation factor, which is a function dependent on wave intrinsic parameters, especially vertical wavelengths (Liu & Swenson, 2003; Hickey & Yu, 2005). For each set of images (two TD images or three raw images), there can be zero to multiple gravity waves identified and counted within this period of triple image in-

Table 1. Number of accumulated hours of OH airglow images captured in each month at ALO.

Year	Jan	Feb	Mar	Apr	May	Jun	Jul	Aug	Sep	Oct	Nov	Dec	**Total**
2009									61.5	49.8	141.9	284.0	537.2
2010	176.7	183.7	213.5	321.5	194.9	128.8	212.7	270.7	120.2			23.5	1846.4
2011	117.7	5.1	30.5	133.7	251.2	238.1	258.7	187.9	161.8	120.4	160.6	210.8	1876.7
2012	66.2	13.3	112.2	13.7	6.4	11.3	233.1	6.5	120.2	35.6	54.5	32.9	705.7
2013		59.9	121.3	107.4		92.0	74.8	27.8	40.9	112.4	63.9	9.0	709.4
2014	120.4	90.5	61.6	90.4	53.0		42.12	80.9					539.0
Total	481.0	352.3	539.1	666.7	505.5	470.3	821.5	573.8	504.6	318.2	420.9	560.2	6214.2

tegration time. There exist some gravity wave events lasting longer time and showing up in multiple sets of images. In our analysis, one persistent wave event will be counted as multiple waves that are retrieved from different sets of TD images. Therefore, the statistics based on wave counts represent the overall duration of gravity waves, not numbers of coherent gravity wave events. However, the statistics of gravity wave events are also analyzed.

There are a few steps in the data processing that need extra attention when discussing results in the following sections. Firstly, the TD method acts as a high-pass filter and excludes stationary and slower wave features such as mountain waves. Therefore, the analysis here only include high frequency gravity waves. The influence of TD method is discussed in details in Support Information. Secondly, in order to find intrinsic wave parameters, the Doppler shift correction is applied after the observed (ground-based) wave parameters are calculated. This is different from the conventional method where the raw images were shifted opposite to the background wind before the wave parameters were estimated (Z. Li et al., 2011). This is to avoid any possible image deterioration in shifting images. Thirdly, some pixels on the imager CCD were broken after Nov 2012 and a black band about 20 km wide showed up in the side of airglow images. The bad pixels were cropped which makes the images used for wave extraction slightly smaller than previously used. This brings little difference in extracted wave parameters since the size of remaining images is still much larger than typical wavelength.

4 Results

4.1 Wave Parameters Statistics

Figure 1 demonstrates the histograms (frequency) for typical gravity wave parameters, including horizontal wavelength, vertical wavelength, observed phase speed, intrinsic phase speed, intrinsic period and wave amplitude. The bin sizes for them are 2.5 km, 2.5 km, 5 ms^{-1}, 5 ms^{-1}, 1 min and 0.1%, respectively. The normalized frequencies are divided by the bin width to make the histograms akin to probablity density functions. In order to evaluate the robustness of the histogram, Bootstrapping method is used to estimate the 95% confidence intervals for each frequency. In this study, the number of identified waves are more than 60000, the histograms are robust as indicated by small statistical uncertainties. The horizontal wavelengths of most waves are less than 100 km

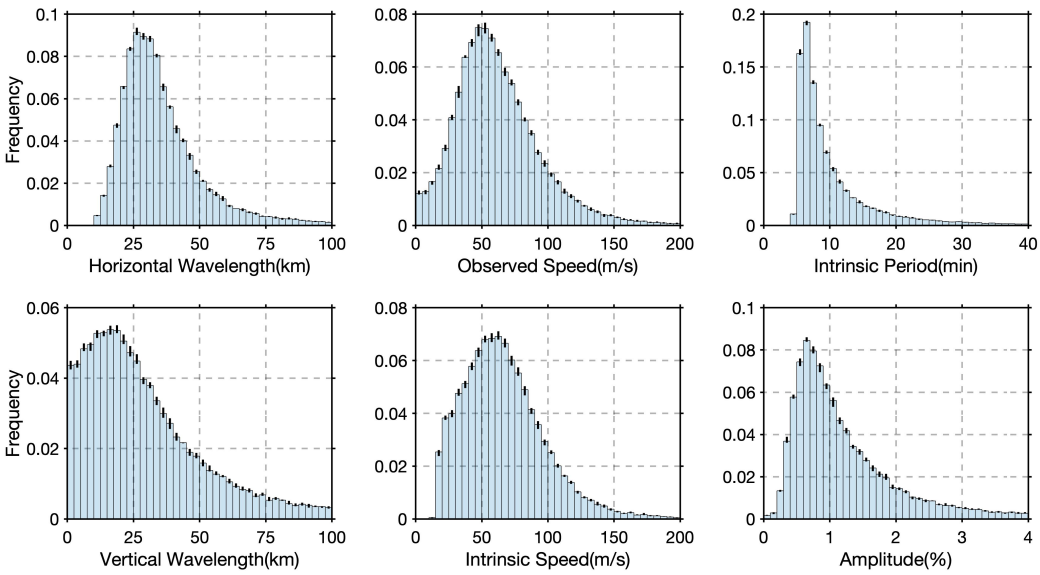

Figure 1. Histograms of gravity wave parameters (from top to bottom, left to right), horizontal wavelength, vertical wavelength, observed phase speed, intrinsic phase speed, period and relative intensity. Small vertical solid lines on top of each bar indicate the 95% confidence interval for each frequency.

with peaks near 20–30 km. The vertical wavelengths are mostly larger than 10 km and with peaks near 15–25 km range. These wavelengths are similar to those found in Maui (Z. Li et al., 2011) and other sites (Taylor et al., 1993; Nakamura et al., 1999; J. H. Hecht et al., 2004; Dou et al., 2010). Due to the cancellation effects of wave perturbations in airglow layer (Liu & Swenson, 2003), waves with vertical wavelength smaller than the thickness of airglow layer will be greatly attenuated in airglow images. As indicated by the calculation of vertical wavelength, most of the waves (84%) identified from airglow images are freely-propagating waves (with positive vertical wavenumber) of which most of waves (81%) has vertical wavelength larger than 10 km. The calculation of vertical wavelength requires background temperature which is retrieved from an empirical model instead of realistic observations. So the distribution of vertical wavelength is treated as reliable only in climatological and statistical perspective. When daily variations are considered, discrepancies are expected. Those waves with very short vertical wavelength ($\leq$10 km) might be due to inaccuracy of the model data. The observed (ground-based) horizontal phase speeds peak near 45–55 ms^{-1}, while intrinsic horizontal phase speeds peak near 60–70 ms^{-1}, which indicates waves mostly propagate against background winds.

For the wave intrinsic period, the short-period (high-frequency) waves dominate with period mostly less than 10 min, with peak near 5–6 min. Due to the fact that most gravity waves propagate against the background wind, the waves are Doppler-shifted to higher intrinsic frequency and large vertical wavelength, which makes high-frequency waves more likely to be observed in airglow images. The wave induced emission intensities are less than 2–3% and peak near 0.5–0.6%.

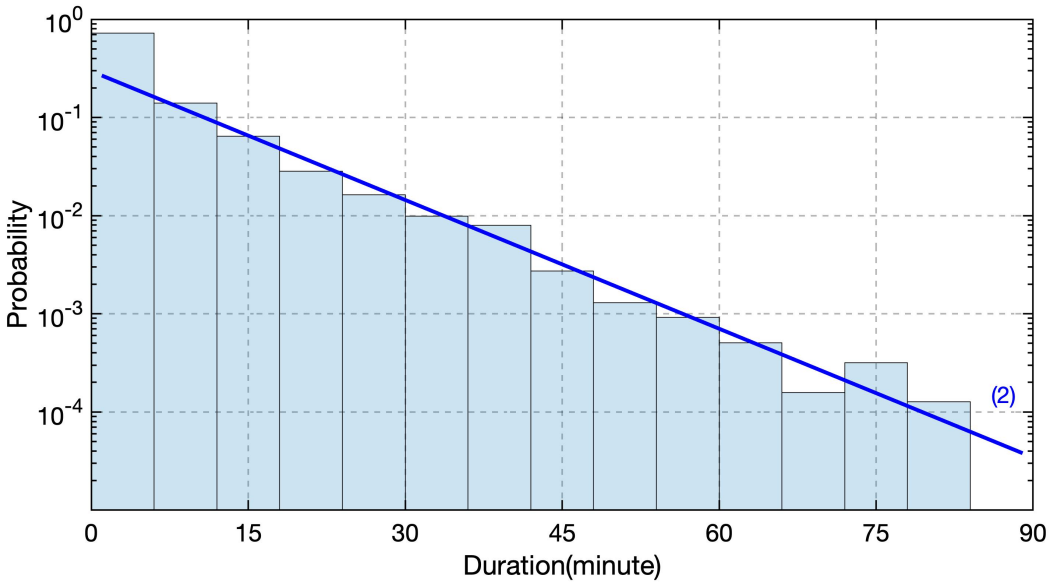

Figure 2. Histogram of the wave event duration. Thick straight lines are from least square fitting. The numbers in the parenthesis at the tails of histograms are the number of wave events at corresponding probabilities.

There exists coherent and persistent 'wave events' lasting longer than the minimum duration of a 'wave', which is the time of a set of three consecutive images. Hereafter, a 'wave event' refers to a coherent gravity wave composed of several consecutive 'waves', which refers to the wave identified from a set of three images. Complete wave events were distinguished by identifying consecutive waves with similar parameters, including propagation direction, wavelength and period. Horizontal propagation azimuth and wavelength/wavenumber were chosen as the primary criteria because they are directly retrieved from 2-D airglow images. After some tentative tests, 15° and 0.001 km^{-1} are chosen as threshold values. After the wave event detection was implemented, most waves were identified as part of a persistent wave event, the remaining waves that do not belong to any wave events were treated as isolated and associated with the minimum duration.

As shown in Figure 2, the probability density function of wave event duration mostly follows an exponential distribution, i.e. a straight line in semi-log coordinate. The wave events associated with the minimum duration fall in the first bin. The longest duration identified from the data is about 80 min. But it is very rare with only 2 wave events identified in more than 6 years. In order to obtain the mathematical function of the probability distribution, a least-square fitting is applied on the histograms based on following formula: $y = \frac{1}{\tau_0} \exp\left(-\frac{x}{\tau_0}\right)$ of which τ_0 and τ_0^2 are the mean and variance for exponential distributions. The fitting was done in semi-log coordinates that a straight line was fitted to find out the slope $(-1/\tau_0)$. Finally, τ_0 is determined as 9.22 min with a 95% confidence interval of 8.28–10.16 min. Theoretically, the mean duration is projected to be 9.22 min for all wave events. However, the actual mean duration of all waves events, including those events with minimum duration, are calculated to be 7.6 min. This is due to the probability of the minimum duration has some derivation from the exponential distribution. Multiple factors such as possible wave breaking, wave packet traversing the imager field-of-view, and wave source characters could contribute to this observed distribution of wave duration. With limited information especially about the background atmosphere status, it is hard to deduce the possible mechanisms that would result in this distribution. Further modeling studies are needed to investigate it in depth.

4.2 Propagation Direction

The distribution of wave characteristics such as wavelenth, period and phase speed does not vary much with seasons. However, the preferential wave propagation directions shows clear seasonal dependence. The distribution of wave propagation and corresponding background wind directions are shown by the histogram in polar coordinate in Figure 3. The histograms are organized by calendar month, four rows are austral summer, fall, winter and spring. There are about 2000–5000 waves identified in each calendar month. Overall, gravity waves tend to propagate against background wind especially during summer and winter time. In summer time (Dec to Feb), the dominant wave propagation direction is mostly southward/polar-ward while the background wind is northward. In winter time (Jun to Aug), the dominant wave propagation direction is northward/equatorward while the winds are southward or southeastward. In spring, the preferential directions show a tendency of transition from northward to southward. Opposite transition

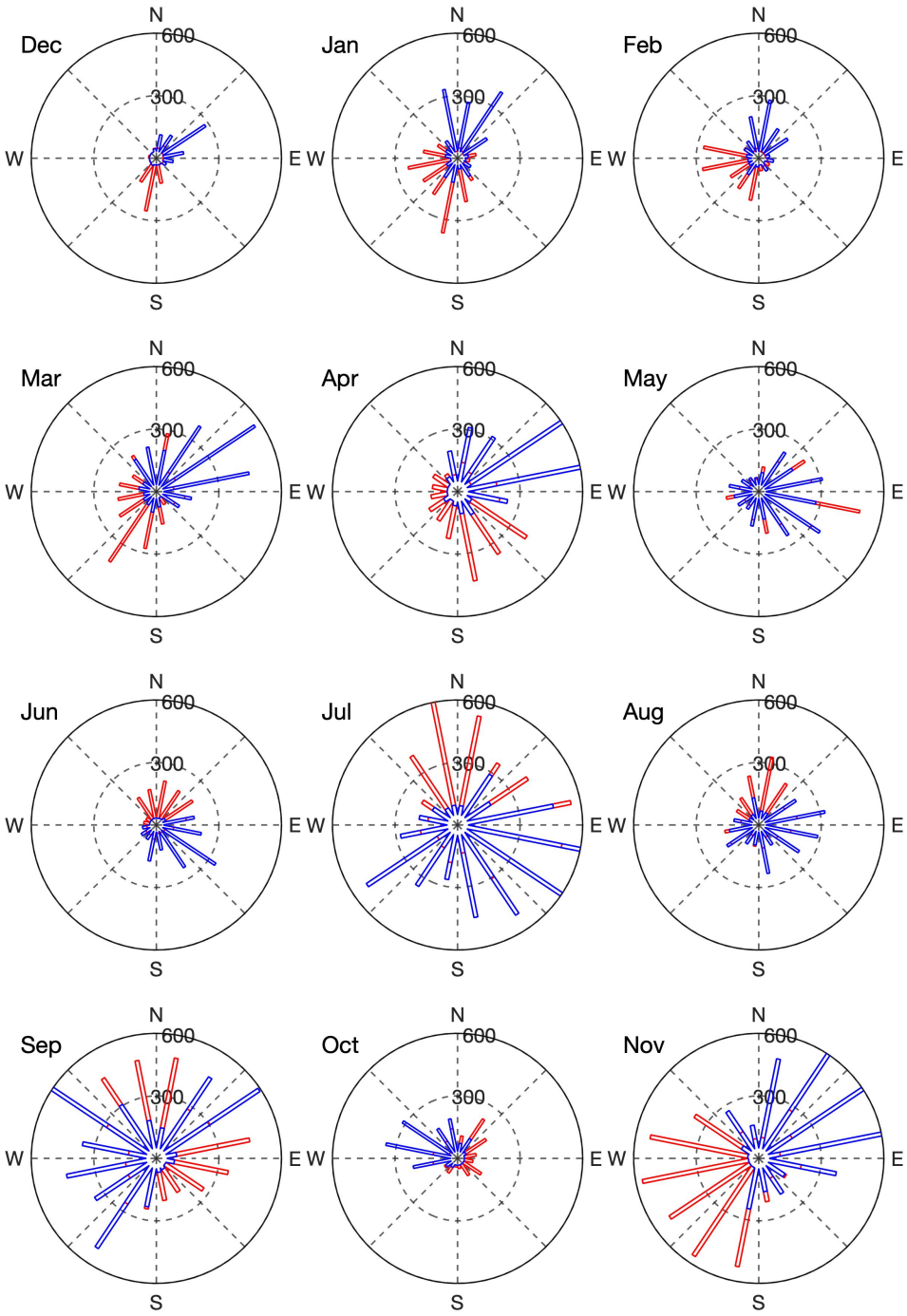

Figure 3. Histograms of (red) wave propagation direction and (blue) background wind direction in each calendar month at a 22.5° azimuth angle bin. The numbers (300, 600) at different radii are the number of waves.

can be found in fall. The preferential propagation direction are contributed by multiple factors including potential wave source locations and background wind filtering.

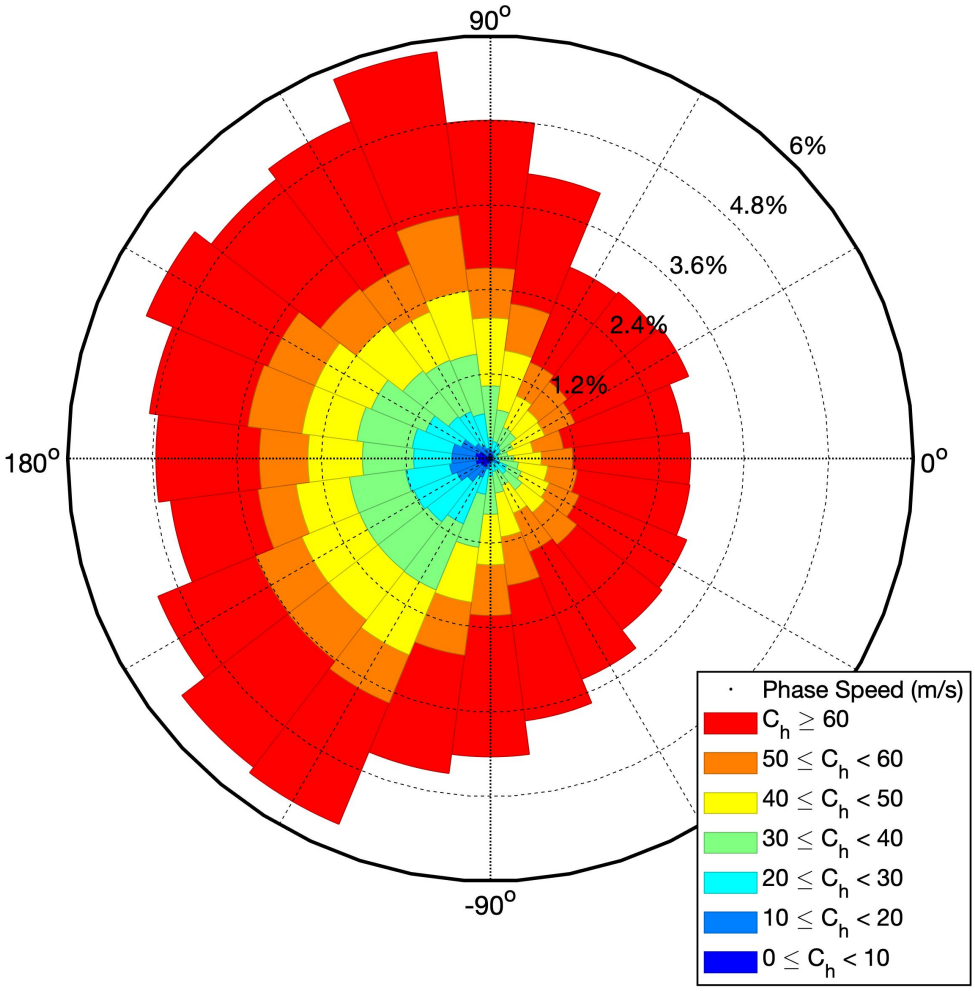

Figure 4. Histogram of azimuth differences between gravity wave propagation and background wind directions for the waves of different observed phase speed. The numbers at different radii are percentage of waves.

In order to evaluate the relationship between propagation and background wind directions of each individual wave, the azimuth angle differences between wave propagation and background wind directions are calculated for waves with different phase speed. As shown in Figure 4, the azimuth angle differences are mostly toward the hemisphere of 180°. However, the distribution have some dependence on the phase speed. For waves with observed phase speed less than 20 ms^{-1}, it is prominent that the azimuth angle dif-

ferences are highly clustered around 180°. This means those waves mostly propagate against the winds which is an indicator of critical layer filtering of waves propagating along the winds if any. The distribution around 180° becomes less concentrated for larger observed phase speeds. For waves with phase speed between 20 and 40 ms^{-1}, they mostly propagate toward opposite direction with background wind but with a boarder range. For those faster waves with phase speed larger than 50 ms^{-1}, their propagation shows little dependence on background wind and can propagate at any directions with respect to background wind. The monthly mean horizontal winds in the OH airglow layer are around 30–40 ms^{-1}. Background winds would be able to filter out waves with observed phase speed similar or smaller than wind speed. However, background winds tend to exert less influence on those faster waves through critical layers filtering. Besides the effects of critical layer, waves propagate along the background winds are Doppler-shifted to smaller vertical wavelength thus larger shear may occur to make waves more easily to break down due to instability. For faster waves, there could be other factors contributing to the preferential propagation direction.

4.3 Background Filtering

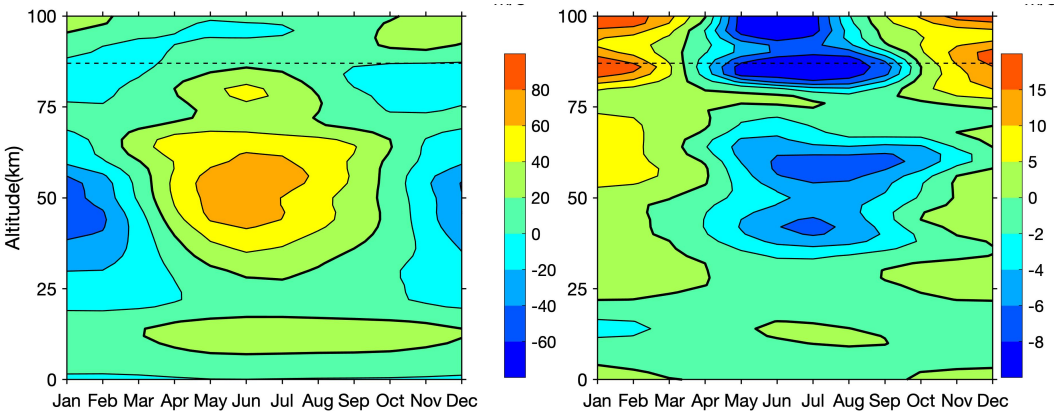

Figure 5. Monthly mean (left) zonal and (right) meridional winds retrieved from HWM-14 model, averaged between 00:00 to 06:00 UT at location of ALO, horizontal dashed lines indicate the mean altitude of OH airglow layer.

Background atmosphere where the waves propagate through plays an important role in controlling the prevailing propagation direction through critical-layer filtering. When gravity waves reach a layer where wave observed phase speed equals background wind

speed, waves will be absorbed or filtered. The Doppler-shifted or intrinsic frequency $\hat{\omega}$ can be related to observed frequency ω by

$$\hat{\omega} = \omega \left(1 - \frac{\overline{u}\cos\phi + \overline{v}\sin\phi}{c} \right), \tag{2}$$

of which the term $\overline{u}\cos\phi + \overline{v}\sin\phi$ is the background wind ($\overline{u}$, $\overline{v}$) projected to wave propagation direction. 'Blocking diagram' (Taylor et al., 1993; Medeiros et al., 2003) is introduced to demonstrate the 'forbidden zone' of gravity waves, i.e., the range of phase speed c and propagation azimuth angle ϕ of waves that would be filtered out in certain background wind profiles where $\hat{\omega} \leq 0$ is satisfied.

Currently, there is no complete observations of atmospheric winds from source level to airglow layer near ALO. We turn to the model winds retrieved from Horizontal Wind Model-14 (HWM-14) (Drob et al., 2015), which reasonably reproduces climatological winds. Figure 5 shows the monthly mean zonal and meridional winds at ALO. Only winds between 00:00 and 06:00 UT are selected to match the timing of airglow images at night. At ALO, zonal winds in the stratosphere are eastward in austral winter and westward in summer, with largest magnitudes excessing ± 60 ms^{-1}. Meridional winds magnitudes are much smaller and are mostly polar-ward but equator-ward in summer above 50 km. In Figure 6, 'blocking diagrams' were plotted for each month using the monthly averaged wind profiles from HWM-14 at ALO. They represent the effects of critical layer filtering on gravity waves accumulated in the altitude range from 15 km that is above most convective activities to 87 km that is the peak altitude of OH airglow. The observed phase speed and propagation direction of all waves are demonstrated by scattered dots. The 'forbidden zones' of gravity waves predicted by critical layer filtering theory are mostly along west and east directions due to much larger amplitudes of zonal wind component especially in stratosphere. As shown in Figure 6, a lot of waves can be found in the predicted 'forbidden zones' in some months. This might be due to the discrepancies between modeled and realistic winds. However, areas around certain smaller phase speeds and directions show up as hollows in the scattered plots in multiple months such as May, Jun, Oct and Nov. The absence of these waves indicates the effects of critical layer filtering, as they are filtered out by the realistic background winds that are not reflected in an empirical wind model.

Here, critical layers filtering predicted by HWM-14 model can not explain the wave propagation direction well. The monthly mean winds retrieved from HWM-14 cannot

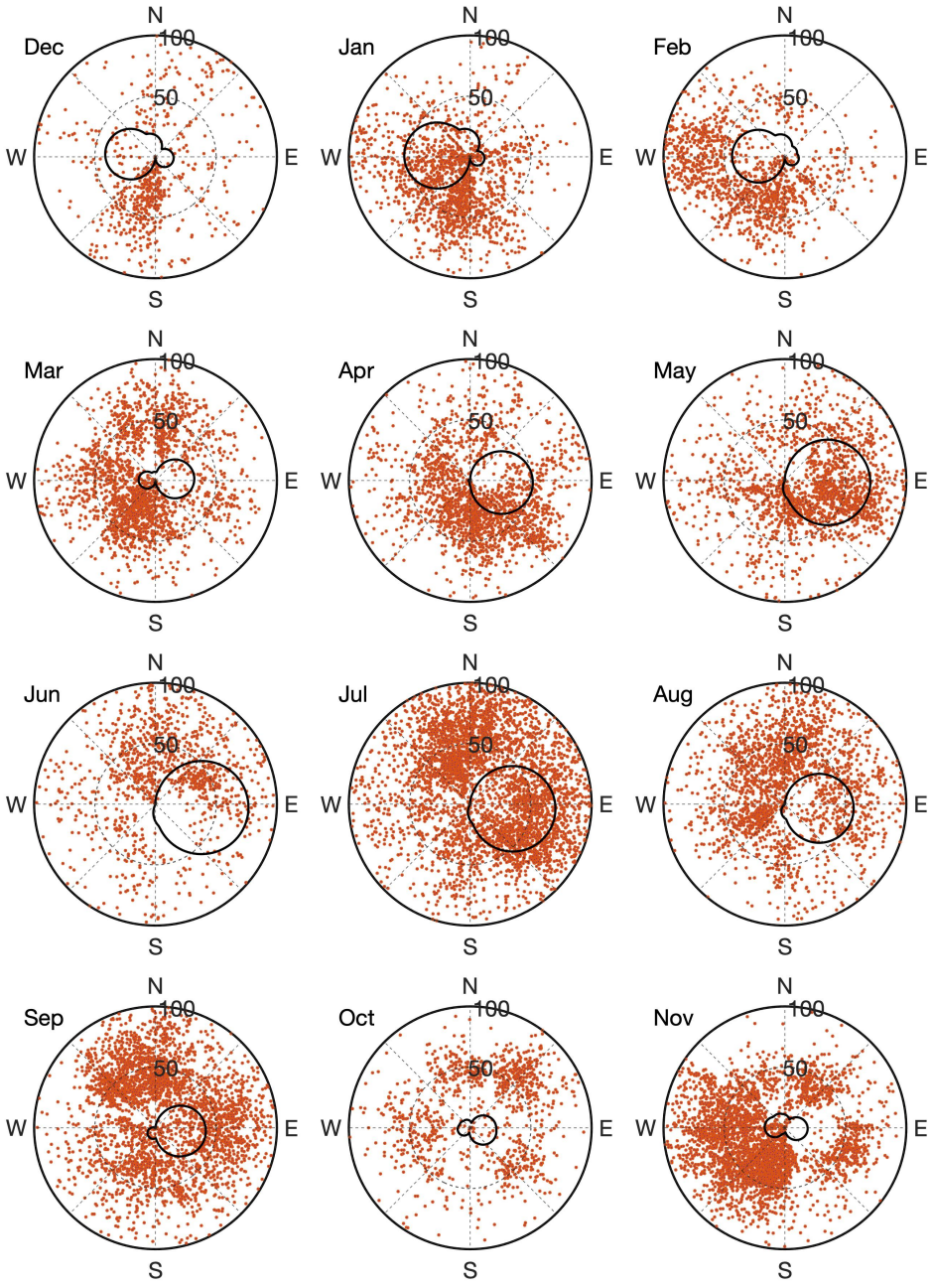

Figure 6. Scatter plots of observed phase speed (0–100 ms^{-1}). One dot represents an identified wave with certain phase speed and propagation direction. Small amount of waves with phase speed larger than 100 ms^{-1} are not included here. Area inside the solid black lines are the 'forbidden zone' predicted by critical layer filtering theory.

capture the short-period variation of the real winds such as tidal influences, day-to-day variability and any waves that have period longer than gravity waves that are observed by airglow imager. Time-varying background winds reduce the effects of critical layer filtering because a lot of waves have less time to interact with varying winds and/or changes of ground phase speed that can be critically filtered (Heale & Snively, 2015). This is especially true for the waves observed by airglow imagers that are mostly high-frequency, with periods less than 15 min.

4.4 Convective Wave Sources

Multiple hot-spots of gravity waves have been revealed by many previous studies using satellite observations and models (Jiang et al., 2004; Geller et al., 2013; Hoffmann et al., 2013, 2016) over the South America and southeast Pacific. Convection and orographic sources were found to be two most likely ones around this region. Vadas, Taylor, et al. (2009) used ray-tracing to locate the potential wave sources and found out the convection is likely the sources of mesospheric gravity waves observed by an OH airglow imager in Brazil.

Outgoing Longwave Radiation (OLR) is a measure of the amount of energy emitted to space from earth's surface, including oceans and atmosphere. OLR values are often used as a good proxy for convection in tropical and subtropical regions. In general, smaller values indicate stronger convective activities because they are associated with high cloud tops with lower temperature. Interpolated monthly mean OLR data (Liebmann & Smith, 1996) was acquired from Physical Sciences Laboratory of NOAA. The data has a 2.5° by 2.5° spatial resolution and global coverage. In Figure 7, the OLR intensities of each month are averaged between 2009 and 2014, and shown by colors with a reversed color-scale. The histogram of propagation direction of gravity waves is also shown on the map. In each calendar month, the occurrence frequency of gravity waves is quantified as the ratio of the number of identified waves to the number of images, which is a proxy of the relative likelihood of occurrence of gravity waves in each months. As shown in Figure 7, the occurrence frequencies are high over winter and early spring(Jun to Oct) and low over summer and fall (Feb to May). Regarding of the wave propagation direction, the occurrence frequency is generally higher when convection is identified at closer distance, especially within 250 km.

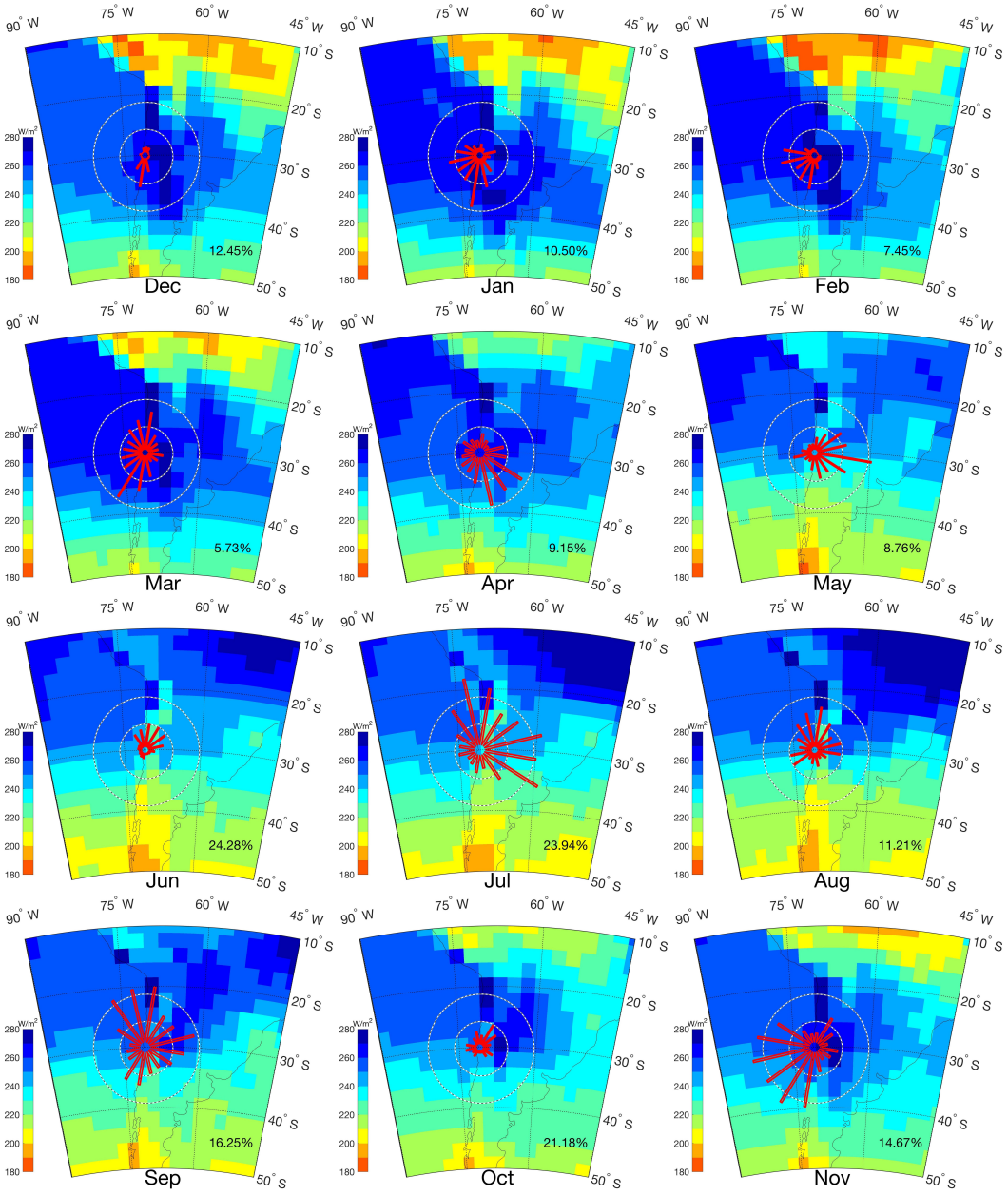

Figure 7. Monthly mean OLR (color shading) overlapped with histograms (in red) on the map showing the coastline of South America. The polar histograms show the propagation direction of gravity waves, same as red in Figure 3. The radius of the two circles centered at ALO represent 250 and 500 waves for histogram. The numbers in the lower right corner of each panel are the wave occurrence frequencies, see text for definition. The color-scale of OLR values is reverse so warmer(red) colors indicate stronger convective activities.

On the continent of South America, there are a few notable areas with strong convection on the north and south side, including Amazon Basin in the tropics and La Palate Basin in the subtropics (∼30°S). They provide a large amount of moisture and energy for deep convection and precipitation (Insel et al., 2010; Romatschke & Houze, 2010). ALO is located on the west side of Andes which has an average elevation of 4–5 km and blocks warm moist air from the east. The convective activities indicated by OLR intensity show clear seasonal variations and high correlations with the wave propagation direction. From late spring to early fall (Nov to Mar), strong convective activities show up in the Amazon Basin and expand to a large area. Some of these convections, especially in summer, are close to ALO within several hundred km. The observed waves have a clear preference of southwestward propagation but with lower occurrence frequencies. In winter (Jun to Oct), the closest and strongest convective source is over the Pacific Ocean to the southwest of ALO and coast area to the south of ALO, during which the wave propagation is clearly northeastward or northward. The convection is much closer to ALO during this time, the occurrence frequencies are highest in a year. From spring to early fall (Sep to Apr), there is also a strong and localized convective source over La Palate Basin to the east and southeast of ALO. This feature is not evident in OLR, but was demonstrated by precipitation and lighting data (Rasmussen et al., 2014, 2016). The wave propagation shows a preference of westward or northwestward in some spring and summer months (Sep, Nov, Jan, Feb, Mar), consistent with this wave source.

4.5 Momentum Fluxes

Figure 8 shows the monthly mean zonal and meridional gravity wave momentum fluxes ($\langle u'w' \rangle$ and $\langle v'w' \rangle$) with zonal and meridional background winds averaged over 22:00–06:00 UT in the OH airglow layer. Overall, the zonal and meridional momentum fluxes have the magnitudes of several m^2s^{-2} with meridional component slightly larger than zonal one. The mean momentum flux magnitudes are very small especially considering the low density in middle atmosphere, each individual wave might not exert large influence on the background. However, a large amount of these waves carrying little momentum flux still show evident effects on the background. Both momentum flux components tend to toward the opposite direction of background winds. Zonal momentum flux is mostly westward and zonal wind is mostly eastward. There are some intra-seasonal variations in zonal momentum flux and wind. The opposite directionality between merid-

ional momentum flux and wind is more distinct. Meridional momentum flux shows a clear annual oscillation with northward maximum near austral winter time and southward maximum in summer. Gravity wave momentum fluxes at mesopause altitude are affected by both wave sources in the lower atmosphere and critical layer filtering by the mean flow between the sources and mesopause (Z. Li et al., 2011). The change of momentum flux is related to the variation of the location of primary wave sources, which are mostly locate at east and northeast of ALO in summer and south in winter. The momentum flux was estimated based on equation 1 using extra information from empirical models, it is also counted as reliable in a climatological perspective.

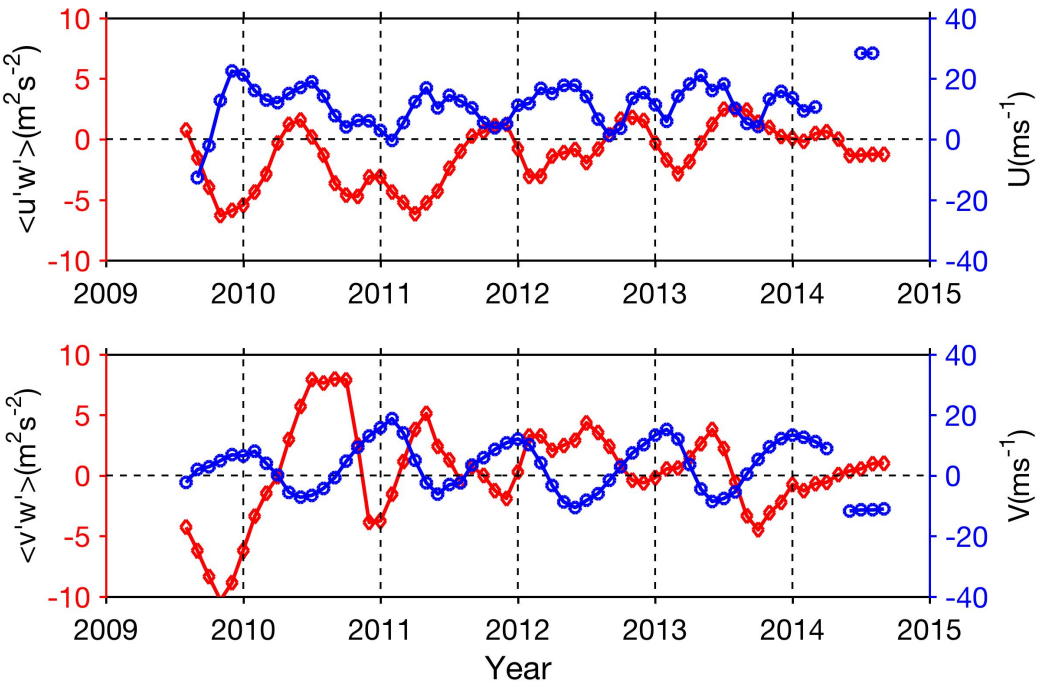

Figure 8. Monthly mean (top) zonal and (bottom) meridional (left axis, red) momentum flux and (right axis, blue) wind from 2009 to 2014. The zonal and meridional winds are averaged between 22:00 to 06:00 UT.

5 Discussions

In the wave extraction method, a set of three consecutive images are used to obtain two TD images for co-spectral analysis. For the airglow imager at ALO, only OH airglow images were captured with a 1-min integration time before 25 Aug 2011 and OH and OI images were captured alternately with 1-min and 1.5-min integration times af-

terwards. A gravity wave event has to last 3 min and 6 min to be identified in these two different configurations (see Figures S1(a) and S1(b)), respectively. For the long term climatology study, in order to minimize the discrepancies due to different integration times, a trade-off made in the data processing is to skip every other image for the time period when only OH airglow images were captured (see Figure S1(c)). The detailed discussions regarding the influences of the TD method and different integration times are presented in the Supporting Information.

In this study, we focus on convection as a primary candidate of wave sources. Clear correlations are revealed between convective activities and observed waves characteristics including wave occurrence frequency and propagation direction. The distance between possible wave source area and ALO where the waves were observed is an important factor. The high-frequency gravity waves tend to propagate upward in a more steep path and thus likely to have a nearby source located within 100–200 km range (Vadas, Yue, et al., 2009). As shown in Figure 7, some intense convective activities in summer time are more than 1000 km away from ALO such as the Amazon Basin in the north and northeast and the area at the east coast of South America. Simulation studies have shown that long-range propagation of gravity waves in MLT region is possible through ducted propagation (J. H. Hecht et al., 2001; Snively & Pasko, 2008; Snively et al., 2013; Heale et al., 2014). However, airglow images retrieved from a single layer could not distinguish whether these waves are ducted. Some of the waves propagating southward and southwestward in late spring and summer (Nov to Mar) are possibly ducted considering the long distance between waves sources and ALO. However, there also exists other wave sources nearby beyond the convection, such as secondary wave generation.

Southern Andes has been reported in many studies as a hot-spot of orograhphically-generated gravity waves. Satellite observations and modeling reveal highest wave occurrence at mid-fall to mid-spring (Apr-Oct) (Hoffmann et al., 2013; Alexander et al., 2015; Hoffmann et al., 2016). The hot-spots concentrate around the west coast of South America along the ridge of Andes, extending from 30°S to the tip at 60°S. It is found that the wave activities are closely correlated with lower-level zonal flow over topography around winter time. Large amount of northward propagating waves are observed in this study with highest occurrence frequencies around the same period over ALO. These waves originate from southern area where the core of the hot-spot is located. Even though these mesospheric high-frequency gravity waves observed by the airglow imager are not directly

generated by orographic sources, there also exist the possibility of secondary wave generation (Vadas et al., 2003; Bossert et al., 2017) due to nonlinear interaction or wave dissipation. Orographic gravity waves have near-zero ground phase speed. They are absorbed and dissipate near the zero-wind layer. As revealed by the monthly mean horizontal winds in Figure 5, there exists zero-wind layers in stratosphere beneath the OH airglow layer between Apr and Sep. Even though the climatological model winds do not capture the short term variations, the background atmosphere is still favorable for the breaking of mountain waves and resulting secondary wave generation in those months.

The discussion of wave-background interaction below the airglow layer altitude is limited because of the use of climatological model winds, which do not duplicate the realistic winds and fully explain the observed results. Further studies utilizing more realistic reanalysis data would be beneficial to evaluate the critical layer filtering, and provide proper background conditions for a ray-tracing modeling study to locate the source area and identify possible ducted propagation. Any waves that cannot be traced back all the way to the troposphere might be accounted to aforementioned mechanisms.

6 Summary and Conclusions

The long-term dataset from 2009 to 2014, retrieved by an all-sky airglow imager at ALO, is used to investigate the characteristics of high-frequency quasi-monochromatic gravity waves. The typical horizontal wavelengths are around 20–40 km and ground-based horizontal phase speeds are between 40 and 70 ms^{-1}. The intrinsic periods of gravity waves cluster around 4–10 min. However, those wave parameters are jointly limited by the 'observation filter' effort of the airglow imager, and the images processing method. And some parameters such as vertical wavelength and momentum flux are estimated using information of empirical models, they are reliable only in statistical and climatological perspective. The observed gravity waves tend to propagate against the local background wind in most months and also show strong seasonal dependence in the preferential propagation direction. The duration of coherent 'wave events' is found to follow an exponential distribution, with a mean duration about 7–9 min. It is not yet fully understood the mechanism that leads to such a distribution. The mean wave momentum flux estimated from airglow data has a much smaller magnitude of several m^2s^{-2} compared to those distinct waves investigated in case studies. However, these waves associated little momentum flux contribute significantly to alter background collectively be-

cause of their much higher probability of presence (Cao & Liu, 2016). The wave momentum flux tends to be toward opposite direction of background winds in airglow layer, especially in meridional direction. These results are consistent with previous studies based on airglow images from other mid-latitude sites such as Fort Collins, CO (20°N) (Y. Tang et al., 2014), Maui, HI (20°N) (Z. Li et al., 2011), Shigaraki, Japan (35°N) (Nakamura et al., 1999) and Urbana, IL (40°N) (J. H. Hecht et al., 2001). In addition to the similarities, the presented wave characteristics especially the preferential propagation direction and occurrence frequency show high correlation with localized environment. The new results add information of high-frequency gravity waves in the mid-latitude of Southern Hemisphere that is beneficial to the understanding of gravity waves in global scale.

It has been suggested that source locations where the waves are generated and background wind where the waves propagate through, cooperatively determine the observed wave characteristics in MLT region. ALO is located at a place near or within the zone of influence of several remarkable convection sources. During the austral summer, the convection over Amazon Basin is dramatically strong and expands over a vast area. Those waves with southwestward propagation direction could originate from there and might be associated with ducted long range propagation. Even the stratospheric zonal wind are mostly westward in this season, the wave sources overwhelm the background wind filtering effect in determining the directionality of wave propagation direction. In winter time, the closer convection is over the Pacific Ocean or coast area to the south of ALO, this could mostly explain the northeastward and northward preferential propagation direction. Critical-layer filtering predicted by model winds could not explain the propagation direction preference well in most months. However, some hollow zones exist in 'block diagram' that indicate the efforts of filtering of the waves with slower velocities. The opposite direction of gravity waves and local background wind also indicates the filtering effects of critical layer on slower waves. The results of this study do not show that the anisotropy of propagation direction was entirely due to wave filtering by stratospheric winds (Taylor et al., 1993; Medeiros et al., 2003) as the background winds exert effects mainly on slower waves. The locations of wave sources and where they are observed play a more important role in shaping the prevailing wave propagation. In this study, the relationship between the observed waves and potential sources is described mostly qualitatively. The relationship between the strength of the convective activities and wave occurrence frequency, wave amplitude can be described with some dependence on distance.

In other words, it could be possible to quantify the influential area of certain convective activities. This would provide some insight regarding a simplified assumption in the gravity wave parameterization that the horizontal propagation of waves are neglected.

Acknowledgments

This research was supported by National Science Foundation (NSF) grant numbers AGS-1110199 and AGS-1759471. The authors sincerely acknowledge Dr. Fabio Vargas and Dr. Gary Swenson of UIUC for their work on radar and imager operation at ALO. The ALO lidar operation was supported by NSF grants AGS-1136278 and AGS-1136208. We are grateful for the excellent support of the ALO facility provided by the Association of Universities for Research in Astronomy (AURA). The OH airglow images from ALO are downloaded from `http://lidar.erau.edu/data/asi/`. The meteor radar data is acquired from `https://zenodo.org/record/4267147`. The OLR data is provided by the NOAA/OAR/ESRL PSL, Boulder, Colorado, USA from their website at `https://psl.noaa.gov/`. The NRLMSISE-00 and HWM-14 models data are generated by functions embedded in Matlab Aerospace Toolbox (`https://www.mathworks.com/products/aerospace-toolbox.html`).

References

Alexander, P., de la Torre, A., Schmidt, T., Llamedo, P., & Hierro, R. (2015). Limb sounders tracking topographic gravity wave activity from the stratosphere to the ionosphere around midlatitude Andes. *Journal of Geophysical Research: Space Physics*, *120*(10), 9014-9022. Retrieved from `https://agupubs.onlinelibrary.wiley.com/doi/abs/10.1002/2015JA021409` doi: 10.1002/2015JA021409

Bossert, K., Fritts, D. C., Pautet, P. D., Taylor, M. J., Williams, B. P., & Pendleton, W. R. (2014). Investigation of a mesospheric gravity wave ducting event using coordinated sodium lidar and Mesospheric Temperature Mapper measurements at ALOMAR, Norway (69°N). *J. Geophys. Res.*, *119*(16), 9765-9778. doi: 10.1002/2014JD021460

Bossert, K., Kruse, C. G., Heale, C. J., Fritts, D. C., Williams, B. P., Snively, J. B., ... Taylor, M. J. (2017). Secondary gravity wave generation over New Zealand during the DEEPWAVE campaign. *Journal of Geophysical Research: Atmospheres*, *122*(15), 7834-7850. Retrieved from `https://`

agupubs.onlinelibrary.wiley.com/doi/abs/10.1002/2016JD026079 doi: 10.1002/2016JD026079

Cao, B., Heale, C. J., Guo, Y., Liu, A. Z., & Snively, J. B. (2016). Observation and modeling of gravity wave propagation through reflection and critical layers above Andes Lidar Observatory at Cerro Pachón, Chile. *Journal of Geophysical Research: Atmospheres*, *121*(21), 12,737–12,750. Retrieved from http://dx.doi.org/10.1002/2016JD025173 doi: 10.1002/2016JD025173

Cao, B., & Liu, A. Z. (2016). Intermittency of gravity wave momentum flux in the mesopause region observed with an all-sky airglow imager. *Journal of Geophysical Research: Atmospheres*, *121*(2), 650–663. Retrieved from http://dx.doi.org/10.1002/2015JD023802 doi: 10.1002/2015JD023802

Dou, X., Li, T., Tang, Y., Yue, J., Nakamura, T., Xue, X., ... She, C.-Y. (2010). Variability of gravity wave occurrence frequency and propagation direction in the upper mesosphere observed by the OH imager in Northern Colorado. *Journal of Atmospheric and Solar-Terrestrial Physics*, *72*(5–6), 457-462. Retrieved from http://www.sciencedirect.com/science/article/pii/S1364682610000131 doi: http://dx.doi.org/10.1016/j.jastp.2010.01.002

Drob, D. P., Emmert, J. T., Meriwether, J. W., Makela, J. J., Doornbos, E., Conde, M., ... Klenzing, J. H. (2015). An update to the Horizontal Wind Model (HWM): The quiet time thermosphere. *Earth and Space Science*, *2*(7), 301-319. Retrieved from https://agupubs.onlinelibrary.wiley.com/doi/abs/10.1002/2014EA000089 doi: https://doi.org/10.1002/2014EA000089

Ejiri, M. K., Shiokawa, K., Ogawa, T., Igarashi, K., Nakamura, T., & Tsuda, T. (2003). Statistical study of short-period gravity waves in OH and OI nightglow images at two separated sites. *J. Geophys. Res.*, *108*(D21). doi: doi:10.1029/2002JD002795

Franke, S. J., Chu, X., Liu, A. Z., & Hocking, W. K. (2005). Comparison of meteor radar and Na Doppler lidar measurements of winds in the mesopause region above Maui, Hawaii. *J. Geophys. Res.*, *110*(D9). doi: 10.1029/2003JD004486

Fritts, D. C., & Alexander, M. J. (2003). Gravity wave dynamics and effects in the middle atmosphere. *Rev. Geophys.*, *41*(1). doi: 10.1029/2001RG000106

Fritts, D. C., Wang, L., Taylor, M. J., Pautet, P.-D., Criddle, N. R., Kaifler, B., ... Liley, B. (2019). Large-Amplitude Mountain Waves in the Meso-

563 sphere Observed on 21 June 2014 During DEEPWAVE: 2. Nonlinear Dy-
564 namics, Wave Breaking, and Instabilities. *Journal of Geophysical Re-*
565 *search: Atmospheres*, *124*(17-18), 10006-10032. Retrieved from `https://`
566 `agupubs.onlinelibrary.wiley.com/doi/abs/10.1029/2019JD030899` doi:
567 https://doi.org/10.1029/2019JD030899

568 Geller, M. A., Alexander, M. J., Love, P. T., Bacmeister, J., Ern, M., Hertzog, A.,
569 ... Zhou, T. (2013). A comparison between gravity wave momentum fluxes
570 in observations and climate models. *Journal of Climate*, *26*(17), 6383–6405.
571 Retrieved from `http://dx.doi.org/10.1175/JCLI-D-12-00545.1` doi:
572 10.1175/JCLI-D-12-00545.1

573 Heale, C. J., & Snively, J. B. (2015). Gravity wave propagation through a verti-
574 cally and horizontally inhomogeneous background wind. *Journal of Geophys-*
575 *ical Research: Atmospheres*, *120*(12), 5931–5950. Retrieved from `http://dx`
576 `.doi.org/10.1002/2015JD023505` doi: 10.1002/2015JD023505

577 Heale, C. J., Snively, J. B., & Hickey, M. P. (2014). Numerical simulation of the
578 long-range propagation of gravity wave packets at high latitudes. *Journal of*
579 *Geophysical Research: Atmospheres*, *119*(19), 11,116–11,134. Retrieved from
580 `http://dx.doi.org/10.1002/2014JD022099` doi: 10.1002/2014JD022099

581 Hecht, J., Walterscheid, R. L., & Vincent, R. A. (2001). Airglow observations of dy-
582 namical (wind shear-induced) instabilities over Adelaide, Australia, associated
583 with atmospheric gravity waves. *J. Geophys. Res.*, *106*(D22), 28189-28197.

584 Hecht, J. H., Kovalam, S., May, P. T., Mills, G., Vincent, R. A., Walterscheid, R. L.,
585 & Woithe, J. (2004). Airglow imager observations of atmospheric gravity waves
586 at Alice Springs and Adelaide, Australia during the Darwin Area Wave Experi-
587 ment (DAWEX). *J. Geophys. Res.*, *109*(D20). doi: 10.1029/2004JD004697

588 Hecht, J. H., Walterscheid, R. L., Hickey, M. P., & Franke, S. J. (2001). Climatology
589 and modeling of quasi-monochromatic atmospheric gravity waves observed over
590 Urbana Illinois. *J. Geophys. Res.*, *106*(D6), 5181–5195.

591 Hickey, M. P., & Yu, Y. (2005). A full-wave investigation of the use of a 'cancella-
592 tion factor' in gravity wave–OH airglow interaction studies. *J. Geophys. Res.*,
593 *110*. doi: 10.1029/2003JA010372

594 Hindley, N. P., Wright, C. J., Smith, N. D., & Mitchell, N. J. (2015). The southern
595 stratospheric gravity wave hot spot: individual waves and their momentum

fluxes measured by COSMIC GPS-RO. *Atmospheric Chemistry and Physics*, *15*(14), 7797–7818. Retrieved from http://www.atmos-chem-phys.net/15/7797/2015/ doi: 10.5194/acp-15-7797-2015

Hocking, W. K., Fuller, B., & Vandepeer, B. (2001). Real-time determination of meteor-related parameters utilizing modern digital technology. *J. Atmos. Sol.-Terr. Phys.*, *63*(2-3), 155-169.

Hoffmann, L., Grimsdell, A. W., & Alexander, M. J. (2016). Stratospheric gravity waves at Southern Hemisphere orographic hotspots: 2003–2014 AIRS/Aqua observations. *Atmospheric Chemistry and Physics*, *16*(14), 9381–9397. Retrieved from https://www.atmos-chem-phys.net/16/9381/2016/ doi: 10.5194/acp-16-9381-2016

Hoffmann, L., Xue, X., & Alexander, M. J. (2013). A global view of stratospheric gravity wave hotspots located with Atmospheric Infrared Sounder observations. *Journal of Geophysical Research: Atmospheres*, *118*(2), 416–434. Retrieved from http://dx.doi.org/10.1029/2012JD018658 doi: 10.1029/2012JD018658

Insel, N., Poulsen, C. J., & Ehlers, T. A. (2010). Influence of the Andes Mountains on South American moisture transport, convection, and precipitation. *Climate Dynamics*, *35*(7), 1477–1492. Retrieved from http://dx.doi.org/10.1007/s00382-009-0637-1 doi: 10.1007/s00382-009-0637-1

Jiang, J. H., Wang, B., Goya, K., Hocke, K., Eckermann, S. D., Ma, J., ... Read, W. G. (2004). Geographical distribution and interseasonal variability of tropical deep convection: UARS MLS observations and analyses. *J. Geophys. Res.*, *209*(D03111). doi: doi:10.1029/2003JD003756

Khomich, V. Y., Semenov, A. I., & Shefov, N. N. (2008). *Airglow as an indicator of upper atmospheric structure and dynamics*. Springer.

Li, J., Li, T., Dou, X., Fang, X., Cao, B., She, C.-Y., ... Thorsen, D. (2017). Characteristics of ripple structures revealed in OH airglow images. *Journal of Geophysical Research: Space Physics*. Retrieved from http://dx.doi.org/10.1002/2016JA023538 doi: 10.1002/2016JA023538

Li, T., She, C. Y., Liu, H.-L., Yue, J., Nakamura, T., Krueger, D. A., ... Wang, S. (2009). Observation of local tidal variability and instability, along with dissipation of diurnal tidal harmonics in the mesopause region over

Fort Collins, Colorado (41 °N, 105 °W). *J. Geophys. Res.*, *114*, D06106, doi:10.1029/2008JD011089. Retrieved from `http://www.agu.org/pubs/crossref/2009/2008JD011089.shtml`

Li, Z., Liu, A. Z., Lu, X., Swenson, G. R., & Franke, S. J. (2011). Gravity wave characteristics from OH airglow imager over Maui. *J. Geophys. Res.*, *116*(D22). doi: 10.1029/2011JD015870

Li, Z., Liu, A. Z., & Sivjee, G. G. (2014). Removing Milky Way from airglow images using principal component analysis. *J. Atmos. Sol.-Terr. Phys.*, *110-111*, 50-57. doi: 10.1016/j.jastp.2014.01.016

Liebmann, B., & Smith, C. A. (1996). Description of a complete (interpolated) outgoing longwave radiation dataset. *Bulletin of the American Meteorological Society*, *77*(6), 1275–1277. Retrieved from `http://www.jstor.org/stable/26233278`

Liu, A. Z., & Swenson, G. R. (2003). A modeling study of O_2 and OH airglow perturbations induced by atmospheric gravity waves. *J. Geophys. Res.*, *108*(D4). doi: 10.1029/2002JD002474

Medeiros, A. F., Takahashi, H., Buriti, R. A., Fechine, J., Wrasse, C. M., & Gobbi, D. (2007). MLT gravity wave climatology in the South America equatorial region observed by airglow imager. *Annales Geophysicae*, *25*(2), 399–406. Retrieved from `https://angeo.copernicus.org/articles/25/399/2007/` doi: 10.5194/angeo-25-399-2007

Medeiros, A. F., Taylor, M. J., Takahashi, H., Batista, P. P., & Gobbi, D. (2003). An investigation of gravity wave activity in the low-latitude upper mesosphere: Propagation direction and wind filtering. *J. Geophys. Res.*, *108*(D14), 4411, doi:10.1029/2002JD002593.

Nakamura, T., Aono, T., Tsuda, T., Admiranto, A. G., Achmad, E., & Suranto. (2003). Mesospheric gravity waves over a tropical convective region observed by OH airglow imaging in Indonesia. *Geophysical Research Letters*, *30*(17). Retrieved from `http://dx.doi.org/10.1029/2003GL017619` doi: 10.1029/2003GL017619

Nakamura, T., Higashikawa, A., Tsuda, T., & Matsushita, Y. (1999). Seasonal variations of gravity wave structures in OH airglow with a CCD imager at Shigaraki. *Earth, Planets and Space*, *51*(7), 897–906. Retrieved from

http://dx.doi.org/10.1186/BF03353248 doi: 10.1186/BF03353248

Picone, J. M., Hedin, A. E., & Drob, D. (2002). NRLMSISE-00 empirical model of the atmosphere: Statistical comparisons and scientific issues. *J. Geophys. Res.*, *107*(A12), SIA 15-1–SIA 15-16. doi: 10.1029/2002JA009430

Rasmussen, K. L., Chaplin, M. M., Zuluaga, M. D., & Houze, R. A. (2016). Contribution of Extreme Convective Storms to Rainfall in South America. *Journal of Hydrometeorology*, *17*(1), 353-367. Retrieved from https://doi.org/10.1175/JHM-D-15-0067.1 doi: 10.1175/JHM-D-15-0067.1

Rasmussen, K. L., Zuluaga, M. D., & Houze Jr., R. A. (2014). Severe convection and lightning in subtropical South America. *Geophysical Research Letters*, *41*(20), 7359-7366. Retrieved from https://agupubs.onlinelibrary.wiley.com/doi/abs/10.1002/2014GL061767 doi: 10.1002/2014GL061767

Romatschke, U., & Houze, R. A. (2010). Extreme summer convection in South America. *Journal of Climate*, *23*(14), 3761-3791. Retrieved from http://dx.doi.org/10.1175/2010JCLI3465.1 doi: 10.1175/2010JCLI3465.1

Snively, J. B., Nielsen, K., Hickey, M. P., Heale, C. J., Taylor, M. J., & Moffat-Griffin, T. (2013). Numerical and statistical evidence for long-range ducted gravity wave propagation over Halley, Antarctica. *Geophysical Research Letters*, *40*(18), 4813–4817. Retrieved from http://dx.doi.org/10.1002/grl.50926 doi: 10.1002/grl.50926

Snively, J. B., & Pasko, V. P. (2008). Excitation of ducted gravity waves in the lower thermosphere by tropospheric sources. *Journal of Geophysical Research: Space Physics*, *113*(A6). Retrieved from http://dx.doi.org/10.1029/2007JA012693 doi: 10.1029/2007JA012693

Swenson, G. R., & Mende, S. B. (1994). OH emission and gravity waves (including a breaking wave) in all-sky imagery from Bear Lake, UT. *Geophysical Research Letters*, *21*(20), 2239–2242. Retrieved from http://dx.doi.org/10.1029/94GL02112 doi: 10.1029/94GL02112

Tang, J., Franke, S. J., Kamalabadi, F., & Swenson, G. R. (2005). Motion extraction of atmospheric waves from spectroscopic imaging. *Geosci. Rem. Sens. Lett.*, *2*(2), 229- 232.

Tang, J., Kamalabadi, F., Franke, S. J., Liu, A. Z., & Swenson, G. R. (2005). Estimation of gravity wave momentum flux using spectroscopic imaging. *IEEE*

Transactions on Geoscience and Remote Sensing, *43*(1), 103-109.

Tang, Y., Dou, X., Li, T., Nakamura, T., Xue, X., Huang, C., ... Avery, S. (2014). Gravity wave characteristics in the mesopause region revealed from OH airglow imager observations over Northern Colorado. *Journal of Geophysical Research: Space Physics*, *119*(1), 630–645. doi: 10.1002/2013JA018955

Taylor, M. J. (1997). A review of advances in imaging techniques for measuring short period gravity waves in the mesosphere and lower thermosphere. *Adv. Space Res.*, *19*(4), 667-676.

Taylor, M. J., Gu, Y. Y., Tao, X., & Gardner, C. S. (1995). An investigation of intrinsic gravity wave signatures using coordinated lidar and nightglow image measurements. *Geophys. Res. Lett.*, *22*(20), 2853-2856. doi: 10.1029/95GL02949

Taylor, M. J., Pautet, P.-D., Fritts, D. C., Kaifler, B., Smith, S. M., Zhao, Y., ... Russell III, J. M. (2019). Large-Amplitude Mountain Waves in the Mesosphere Observed on 21 June 2014 During DEEPWAVE: 1. Wave Development, Scales, Momentum Fluxes, and Environmental Sensitivity. *Journal of Geophysical Research: Atmospheres*, *124*(19), 10364-10384. Retrieved from `https://agupubs.onlinelibrary.wiley.com/doi/abs/10.1029/2019JD030932` doi: https://doi.org/10.1029/2019JD030932

Taylor, M. J., Ryan, E. H., Tuan, T. F., & Edwards, R. (1993). Evidence of preferential directions for gravity wave propagation due to wind filtering in the middle atmosphere. *Journal of Geophysical Research: Space Physics*, *98*(A4), 6047–6057. doi: 10.1029/92JA02604

Vadas, S. L., Fritts, D. C., & Alexander, M. J. (2003). Mechanism for the generation of secondary waves in wave breaking regions. *Journal of the Atmospheric Sciences*, *60*(1), 194–214. doi: 10.1175/1520-0469(2003)060⟨0194:MFTGOS⟩2.0.CO;2

Vadas, S. L., Taylor, M. J., Pautet, P.-D., Stamus, P. A., Fritts, D. C., Liu, H.-L., ... Takahashi, H. (2009). Convection: the likely source of the medium-scale gravity waves observed in the OH airglow layer near Brasilia, Brazil, during the SpreadFEx campaign. *Annales Geophysicae*, *27*(1), 231–259. doi: 10.5194/angeo-27-231-2009

Vadas, S. L., Yue, J., She, C.-Y., Stamus, P. A., & Liu, A. Z. (2009). A model

728 study of the effects of winds on concentric rings of gravity waves from a con-
729 vective plume near Fort Collins on 11 May 2004. *J. Geophys. Res.*, *114*. doi:
730 10.1029/2008JD010753
731 Walterscheid, R. L., Hecht, J. H., Vincent, R. A., Reid, I. M., Woithe, J., & Hickey,
732 M. P. (1999). Analysis and interpretation of airglow and radar observations of
733 quasi-monochromatic gravity waves in the upper mesosphere and lower ther-
734 mosphere over Adelaide, Australia (35°S, 138°E). *J. Atmos. Sol.-Terr. Phys.*,
735 *61*, 461-478.